

Recommended implementation of electrical resistance tomography for conductivity mapping of metallic nanowire networks using voltage excitation

Original

Recommended implementation of electrical resistance tomography for conductivity mapping of metallic nanowire networks using voltage excitation / Cultrera, A.; Milano, G.; De Leo, N.; Ricciardi, C.; Boarino, L.; Callegaro, L.. - In: SCIENTIFIC REPORTS. - ISSN 2045-2322. - ELETTRONICO. - 11:1(2021), p. 13167. [10.1038/s41598-021-92208-w]

Availability:

This version is available at: 11583/2913492 since: 2021-07-16T17:50:56Z

Publisher:

Nature Research

Published

DOI:10.1038/s41598-021-92208-w

Terms of use:

This article is made available under terms and conditions as specified in the corresponding bibliographic description in the repository

Publisher copyright

(Article begins on next page)



OPEN

Recommended implementation of electrical resistance tomography for conductivity mapping of metallic nanowire networks using voltage excitation

Alessandro Cultrera^{1✉}, Gianluca Milano^{2,3}, Natascia De Leo², Carlo Ricciardi³, Luca Boarino² & Luca Callegaro¹

The knowledge of the spatial distribution of the electrical conductivity of metallic nanowire networks (NWN) is important for tailoring the performance in applications. This work focuses on Electrical Resistance Tomography (ERT), a technique that maps the electrical conductivity of a sample from several resistance measurements performed on its border. We show that ERT can be successfully employed for NWN characterisation if a dedicated measurement protocol is employed. When applied to other materials, ERT measurements are typically performed with a constant current excitation; we show that, because of the peculiar microscopic structure and behaviour of metallic NWN, a constant voltage excitation protocols is preferable. This protocol maximises the signal to noise ratio in the resistance measurements—and thus the accuracy of ERT maps—while preventing the onset of sample alterations.

Electrical Resistance Tomography (ERT, and its counterpart in the ac regime, Electrical Impedance Tomography, EIT^{1–3}) is a technique that determines a spatial map of the conductivity of an object by performing electrical resistance measurements between electrodes on its boundary. ERT was originally developed as a tool for physiology monitoring⁴ and earth science⁵, but later it has been successfully applied to the electrical characterisation of silicon wafer for electronics⁶, composite materials⁷, thin films⁸ and graphene⁹. ERT can provide accurate quantitative results in simple implementations with commercial instrumentation^{8,9}; with dedicated hardware, it can reach a refresh speed in the ms range¹⁰. At the best of our knowledge, to date little evidence of electrical mapping of metallic nanowire networks (NWN) is available in literature¹¹. On the contrary, a fast, non-destructive and traceable characterisation method like ERT would contribute to the establishment of novel NWN based technology. In fact, NWN have already attracted great interest as emerging transparent conductive materials, combining high transparency and flexibility with high electrical conductivity^{12–17}. Consequently, these networks are being investigated for the development of transparent electrodes for photovoltaic applications^{18,19}, transparent heaters²⁰, flexible electronics²¹, but also for the realization of next-generation electronic devices exploiting the reconfigurability of NWN under electrical excitation^{22–24}. These applications require the characterisation of the spatial homogeneity of the electrical properties of NWN at the mm scale or larger. In this sense ERT can become relevant for the development of reliable network-based electrodes and devices. Indeed, differently from in-line four-probe and van der Pauw measurements, ERT can provide information on local electrical properties. Typical ERT implementations, and also the one discussed in this work, allow for mapping the conductivity of samples at the mm scale. So ERT can complement, for example, conductive probe microscopy techniques²⁵, that are usually exploited for conductivity mapping at the micro-nano scale, and other more recent mapping techniques such as the 1-probe mapping¹¹. Moreover, since ERT is a non-scanning technique, the measurement time depends only on the number of contacts placed on the sample's edge and not on the sample size, so in principle it can be

¹Quantum Metrology and Nanotechnologies, INRIM - Istituto Nazionale di Ricerca Metrologica, 10135 Turin, Italy. ²Advanced Materials Metrology and Life Sciences, INRIM - Istituto Nazionale di Ricerca Metrologica, 10135 Turin, Italy. ³Department of Applied Science and Technology, Politecnico di Torino, 10129 Turin, Italy. ✉email: a.cultrera@inrim.it

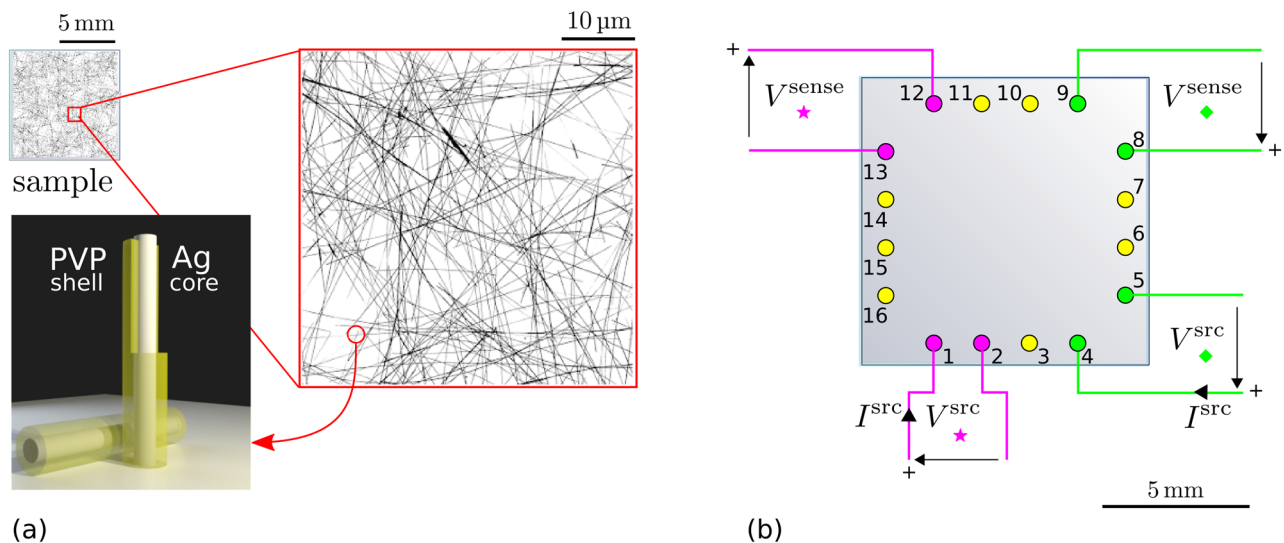


Figure 1. Nanowire network sample on quartz support: illustration of the $1 \times 1 \text{ cm}^2$ sample, SEM micro-graph detail of one of the studied samples and a pictorial representation of PVP-Ag nanowires (a). Schematic representation of the placement of the contact array over the sample. Two examples of ERT four-terminal resistance measurements configurations are shown with the corresponding excitation and sensing quantities (b).

scaled to map even larger NWN samples. At present, examples of ERT on other materials with samples of up to 20 cm lateral size have been successfully proposed^{6,7}.

However, the implementation of ERT for the characterisation of this kind of nanomaterial requires particular attention to the measurement protocol since NWN can be altered by the same electrical stimulation required for their characterisation²³. In fact the possible onset of local high electric fields during the measurements can lead to structural and morphological changes in nanowires (NW) and nanowire junctions (NW-junctions) due to electromigration phenomena, with consequent alteration of the electrical properties of the network^{26–28}. In this work we show that (i) ERT can be successfully applied to measure conductivity maps of Ag NWN coatings; (ii) the typical implementation of ERT, which uses a constant current excitation, can very likely alter the samples even at low current levels, and (iii) an alternative ERT implementation, using a constant voltage excitation, is required when dealing with NWN. Moreover, while guidelines for the correct implementation of ERT in other fields are available^{29,30}, a dedicated study in the field of nanostructured materials like NWN is still missing.

Results

We used NWN made of silver nanowires grown by polyol synthesis process, drop-casted over quartz insulating substrates of $1 \times 1 \text{ cm}^2$ in size (details in the experimental section “Methods”), resulting in a NWN with a highly interconnected morphology as shown in Fig. 1a. The measurements were performed within a few hours from the synthesis of the samples, to minimize possible degradation effects due to ambient exposure, which were previously observed to be negligible on this time scale³¹, and also are limited by the presence of the PVP shell³².

ERT conductivity maps are recovered performing a series of four-terminal transresistance measurements at the sample boundary, of the same type of those involved in the well-known van der Pauw³³ method, and using a finite element model. Measurement and numerical methods are described in section “Methods” (see respectively the paragraphs ERT measurements and ERT modelling). The sample is contacted with an array of n probes at the sample boundary, see Fig. 1b.

In ERT, a set of N four-terminal resistance measurements

$$R_{i,j;k,l} = \frac{V_{k,l}^{sense}}{I_{i,j}^{src}} \quad (1)$$

are performed, where $V_{k,l}^{sense}$ is the voltage at contacts k, l and $I_{i,j}^{src}$ the current flowing through contacts i, j .

In our application $n = 16$, and we adopted the so-called *adjacent* measurement pattern⁴, which involves $N = n \times (n - 3) = 208$ transresistance measurements. The typical ERT implementation² adopts a *constant current* protocol (\mathcal{I}_c in the following): a current generator is set to source a constant current I , and is switched through all contact pairs, thus $I_{i,j}^{src} = I$; the corresponding excitation voltage (often not measured) is $V_{i,j}^{src}$. $V_{k,l}^{sense}$ are measured by a switched voltmeter, or by several in parallel. We experimented also a *constant voltage* protocol (\mathcal{V}_c in the following): a constant excitation voltage $V_{i,j}^{src} = V$ is employed, and the corresponding current $I_{i,j}^{src}$ is measured by an additional ammeter in the setup. $V_{k,l}^{sense}$ are measured like in the \mathcal{I}_c protocol. The choice of the excitation amplitude (I for the \mathcal{I}_c protocol, V for \mathcal{V}_c) has effects both on the signal to noise ratio of the measurements, and on the occurrence of possible reconfiguration events in the NWN, as discussed in the following.

To make a consistent comparison between the two protocols \mathcal{I}_c and \mathcal{V}_c , we can consider the total electrical energy E dissipated in the overall ERT measurement involving N transresistances:

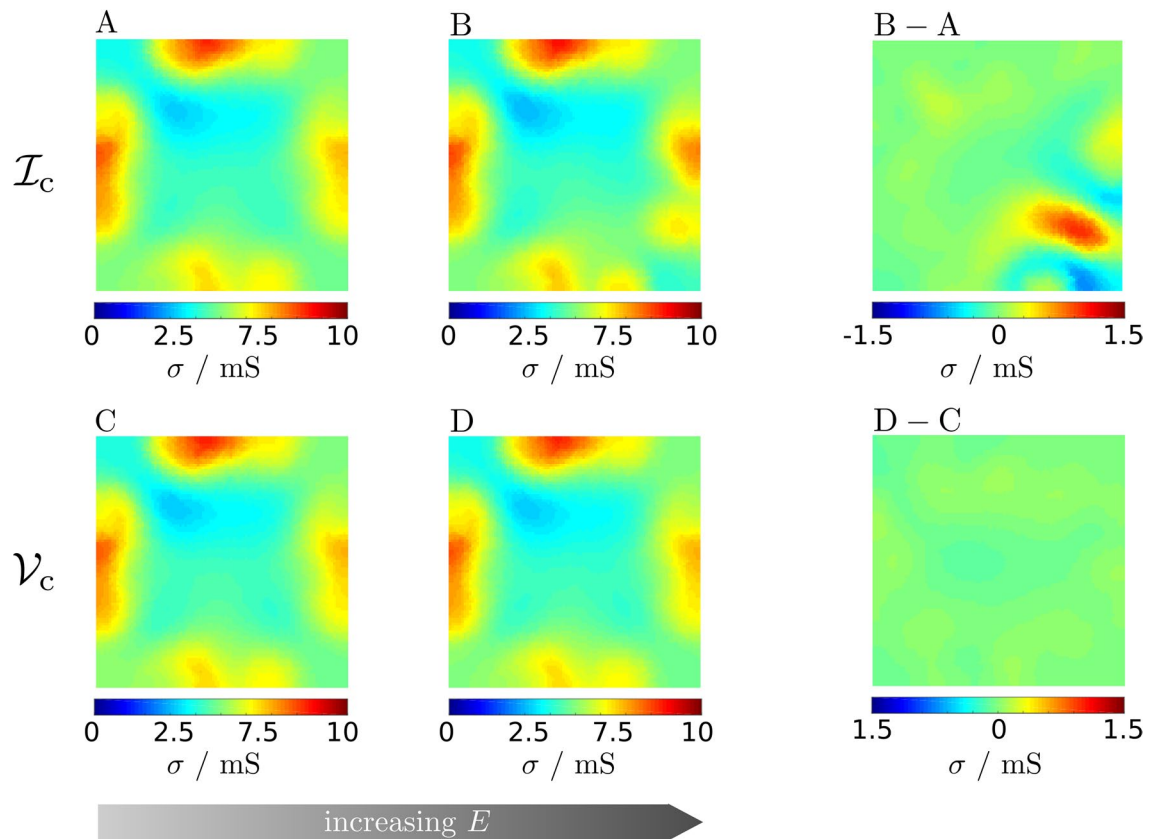


Figure 2. ERT electrical conductivity maps of sample **S** obtained with measurement protocols \mathcal{I}_c (constant current) and \mathcal{V}_c (constant voltage) at increasing excitation energy E . Maps **A** and **C** correspond to low sample excitation energy $E < 55 \mu\text{J}$, while maps **B** and **D** correspond to higher sample excitation energy $E > 5.5 \mu\text{J}$. Map difference **B** – **A** and **D** – **C** show the pixel-by-pixel absolute difference between the corresponding conductivity maps.

$$\begin{aligned}
 E &= \sum_{m=1}^N V_{ij}^{\text{src}} I_{ij}^{\text{src}} T \\
 &= IT \sum_{m=1}^N V_{ij}^{\text{src}} \quad \mathcal{I}_c \\
 &= VT \sum_{m=1}^N I_{ij}^{\text{src}} \quad \mathcal{V}_c,
 \end{aligned} \tag{2}$$

where T is the sample excitation time per individual transresistance measurement. E determines the signal to noise ratio of the overall ERT measurement.

For the ERT reconstruction process, the N transresistances given by Eq. (1) are casted in a vector $\mathbf{R} = [R_{ij;k,l}]$ (see Fig. 3a). The conductivity map σ is the solution of the variational problem

$$\sigma = \arg \min_{\varsigma} (\|\mathbf{R}_{\text{calc}}(\varsigma) - \mathbf{R}\|^2), \tag{3}$$

where $\mathbf{R}_{\text{calc}}(\varsigma)$ is the vector of transresistances calculated using the guess conductivity distribution ς and $\|\bullet\|$ is the Euclidean norm operator. Equation (3) is solved numerically.

We performed ERT measurements on several samples with both protocols \mathcal{I}_c and \mathcal{V}_c and increasing E levels, starting from $E \approx 3 \mu\text{J}$; below this value transresistance measurements resulted too noisy to perform meaningful reconstructions.

Figure 2 reports four ERT conductivity maps, **A**, **B**, **C** and **D**, on a sample of areal mass density (AMD) 105 mg m^{-2} , named **S** in the following. The maps shown in the following reflect the peculiar NW distribution occurred on the considered sample, see Supplementary S3 for an example of a sample that shown a different conductivity distribution.

Measurement conditions are summarized in Table 1. Maps **A** and **B** were retrieved from measurements performed with protocol \mathcal{I}_c ; maps **C** and **D** with protocol \mathcal{V}_c . The measurement parameters are given in Table 1.

| ERT map | Protocol | Excitation | | E | $\delta_{X,Y}/\%$ |
|---------|-----------------|-----------------------|--|--------------------|-----------------------|
| A | \mathcal{I}_c | $I = 10 \mu\text{A}$ | $\max(V^{\text{src}}) = 15 \text{ mV}$ | $29.9 \mu\text{J}$ | – |
| B | \mathcal{I}_c | $I = 400 \mu\text{A}$ | $\max(V^{\text{src}}) = 331 \text{ mV}$ | 7.8 mJ | $\delta_{B,A} = 3.50$ |
| C | \mathcal{V}_c | $V = 5 \text{ mV}$ | $\max(I^{\text{src}}) = 124 \mu\text{A}$ | $25.5 \mu\text{J}$ | $\delta_{C,A} = 0.59$ |
| D | \mathcal{V}_c | $V = 100 \text{ mV}$ | $\max(I^{\text{src}}) = 780 \mu\text{A}$ | 7.1 mJ | $\delta_{D,C} = 0.69$ |

Table 1. ERT settings and relevant quantities corresponding to the sample **S**. For each map shown in Fig. 2 are reported: the protocol, the excitation quantities, the total energy dissipated during the measurement and the map difference with respect to the chosen reference.

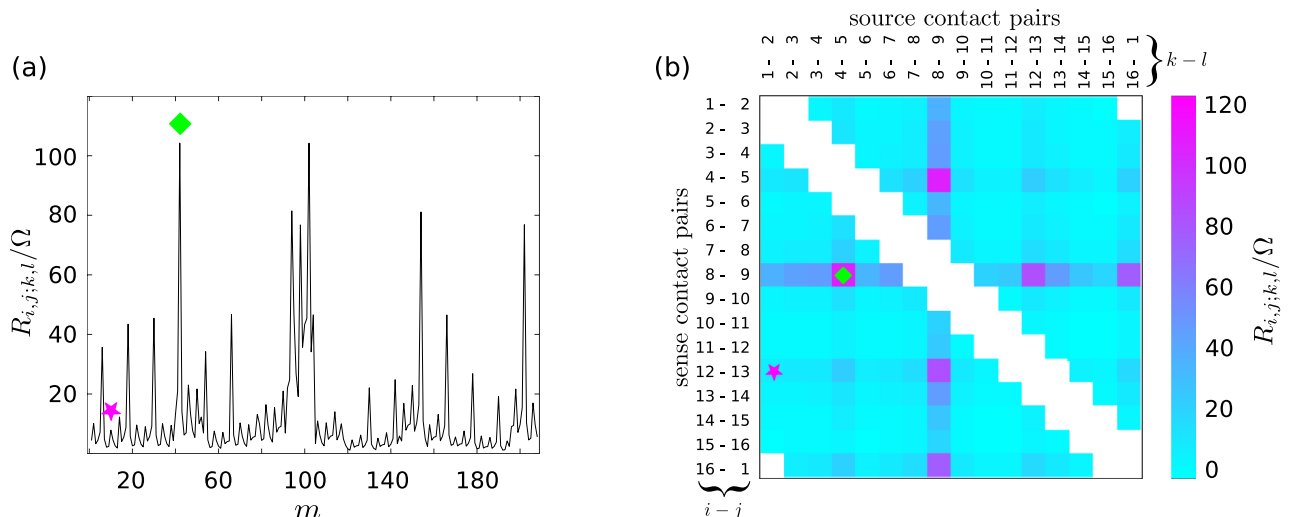


Figure 3. Representations of ERT data of the sample **S**. Plot of \mathbf{R} relative to the map **A** in Fig. 2a. The same data represented as an impedance matrix \mathbf{Z} (b). The diamond and star markers indicates the values of $R_{i,j;k,l}$ measured with the corresponding contact configurations shown in the scheme in Fig. 1b. Due to the measurements arrangement in the plot (a), the symmetry of the data is not evident as it happens looking at \mathbf{Z} in (b).

Map **A** was obtained with protocol \mathcal{I}_c using a low excitation energy $E = 29.9 \mu\text{J}$. The conductivity spans from 3.2 to 8.3 mS; the map average value, 5.04 mS, is consistent with other works³⁴. Map **C** was obtained with protocol \mathcal{V}_c , also with a low excitation energy $E = 25.5 \mu\text{J}$. Maps **C** and **A** are very similar, as can be quantified by the norm of the pixel-by-pixel difference $\delta_{XY} = \frac{\|\mathbf{X}-\mathbf{Y}\|}{\|\mathbf{Y}\|}$, where $\|\bullet\|$ is the sum of the square of the conductivity (or conductivity difference) of each pixel (Frobenius norm), of only $\delta_{CA} = 0.59\%$ between maps **C** and **A**. Protocols \mathcal{I}_c and \mathcal{V}_c gave equivalent results when performed at $E \approx 10 \mu\text{J}$ on sample **S**.

Maps **B** and **D** correspond to measurements performed with a higher excitation energy, potentially of interest to improve the measurement signal to noise ratio, and hence the ERT map accuracy. Map **B** was obtained with protocol \mathcal{I}_c with $E = 7.8 \text{ mJ}$. The difference with map **A** can be visually appreciated; Fig. 2 shows the map relative difference $\mathbf{B} - \mathbf{A}$, which is up to of 20%, with $\delta_{BA} = 3.50\%$. Map **D** was obtained using protocol \mathcal{V}_c and $E = 7.1 \text{ mJ}$, very close to that employed for map **B**. By the way, the map relative difference $\mathbf{D} - \mathbf{C}$ ranges within 1.3%, with a map difference as low as $\delta_{DC} = 0.69\%$. To summarize, maps **A**, **C** and **D** are very similar; only map **B** shows a substantial deviation. Protocols \mathcal{I}_c and \mathcal{V}_c gave no more equivalent results when performed on **S** at excitation energy $E > 2.6 \text{ mJ}$.

A more direct analysis of the effect of the application of protocols \mathcal{I}_c or \mathcal{V}_c at different E levels can be made by considering the measured transresistances. Figure 3a shows a plot of the values $R_{i,j;k,l}$ corresponding to map **A** of Fig. 2; index $m = 1 \dots N$ is the sequential index. The specific $R_{i,j;k,l}$ measured with the adjacent pattern correspond to contact configurations following the rules $j = i + 1$ and $l = k + 1$ (with the convention that $n + 1 \equiv 1$), and can be recast in a matrix \mathbf{Z} having as elements

$$Z_{ik} = R_{i,i+1;k,k+1} \quad i, j = 1 \dots n. \quad (4)$$

\mathbf{Z} for map **A** is shown in Fig. 3b. The $N = 208$ measurements leave some elements of the 16×16 matrix undefined; these correspond to two- or three-terminal measurement configurations which are not considered in ERT because they include the probe to sample contact resistances. In Fig. 3b a strong symmetry of \mathbf{Z} respect to the diagonal can be visually appreciated.

The elements of \mathbf{Z} symmetric respect to the diagonal, $Z_{pq} = R_{p,p+1;q,q+1}$ and $Z_{qp} = R_{q,q+1;p,p+1}$ correspond to configurations where source and sense terminals are swapped. The contacted sample can be considered a

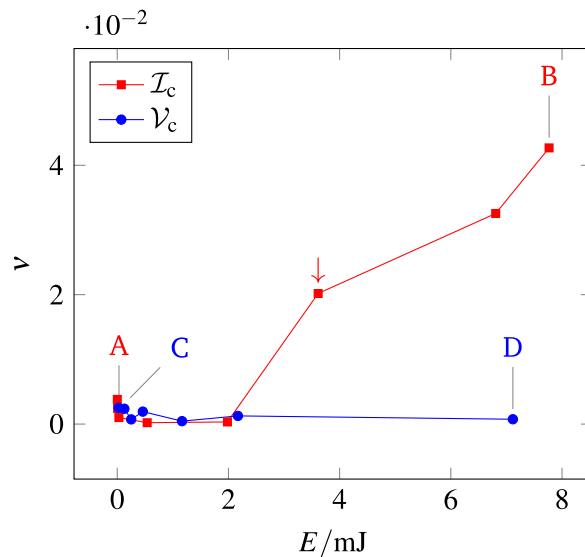


Figure 4. The symmetry index ν of sample S calculated from ERT measurements for increasing E performed at \mathcal{I}_c (—■—) and \mathcal{V}_c (—●—). Letters and arrow label the values of ν corresponding to the maps shown and discussed in the text.

multiterminal electrical passive network, for which the reciprocity theorem³⁵ $Z_{pq} \equiv Z_{qp}$ holds; hence, \mathbf{Z} must be symmetric. Any deviation from symmetry is an indication of measurement errors, or alterations of the sample electrical properties caused by the measurement process. Let us quantify the overall asymmetry of a generic \mathbf{Z} . Since \mathbf{Z} is square, the Toeplitz decomposition in a symmetric and skew-symmetric matrices applies:

$$\mathbf{Z} = \frac{1}{2}(\mathbf{Z} - \mathbf{Z}^T) + \frac{1}{2}(\mathbf{Z} + \mathbf{Z}^T), \quad (5)$$

A symmetry index ν can be introduced as

$$\nu = \frac{\|\mathbf{Z} - \mathbf{Z}^T\|}{\|\mathbf{Z} + \mathbf{Z}^T\|}, \quad (6)$$

where $\|\bullet\|$ indicates a Frobenius norm, evaluated on the available \mathbf{Z} entries. ν is dimensionless and ≥ 0 ; if \mathbf{Z} is symmetric, then $\nu = 0$, and it increases with increasing asymmetry.

Figure 4 plots the asymmetry index ν as a function of E , ranging between 18 μJ and 7.8 mJ, for the two measurement protocols \mathcal{I}_c and \mathcal{V}_c . The values of ν corresponding to maps A, B, C, D of Fig. 2 are marked with letters.

Discussion

The ν values corresponding to the \mathcal{V}_c protocol stay close to zero (hence, \mathbf{Z} is symmetric) in the whole energy range investigated. Considering the \mathcal{I}_c protocol instead, ν is close to zero up to a critical energy $E_{\text{crit}} \approx 0.8$ mJ, after which it ramps up, indicating an increasing asymmetry of \mathbf{Z} .

Figure 4 is consistent with Fig. 2: while maps A, C and D, all three corresponding to $\nu \approx 0$, are very similar one another, the map B, which shows differences, correspond to $\nu > 0$. The asymmetric \mathbf{Z} of map B indicates an alteration occurring *in the course* of the measurement; note that if the sample became altered *during* the ERT measurement, then map B does not even represent a meaningful reconstruction of the conductivity distribution over the sample. To better show how changes in the actual ERT measurements (\mathbf{Z} of Fig. 3) produce changes in the conductivity maps shown in Fig. 2, in Supplementary S2 we reported the matrices \mathbf{Z} corresponding to the four maps A, B, C, D, the differences $\mathbf{B} - \mathbf{A}$ and $\mathbf{D} - \mathbf{C}$.

It is noteworthy that I^{src} is not a good parameter to express an alteration threshold: considering the values of I^{src} achieved at maximum E (see Table 1), the maximum I^{src} applied in the \mathcal{V}_c protocol is 780 μA (case D), while for the \mathcal{I}_c protocol it is of only 400 μA (case B).

When performing measurements with \mathcal{I}_c protocol, the value of E_{crit} has an intrinsic variability, likely dependent on the NWN individual morphology. Measurements performed on other samples found NWN of AMD ≈ 85 mg m^{-2} with E_{crit} spanning between 500 μJ and 2 mJ; for samples with AMD ≈ 115 mg m^{-2} , between 4.5 mJ and 14.5 mJ, a result consistent with a denser network. To this large variability corresponded different ERT maps, corroborating the fact that the individual NW distribution is relevant for the value of E_{crit} . The measurements performed with \mathcal{V}_c protocol on these samples, instead, showed $\nu \approx 0$ within the whole corresponding energy span. Additionally we observed that also measurements on samples of AMD ≈ 150 mg m^{-2} , even though less systematically, showed the same criticality concerning the \mathcal{I}_c protocol, indicating that the \mathcal{V}_c protocol is recommended also for the characterisation of higher AMD NWN.

The observed sample alterations can be related to a reconfiguration of the NWN associated with electromigration phenomena occurring at the nanowire junctions. In fact, it has been extensively reported^{23,27,28,36} that applied voltage above a threshold around 100 mV leads to dissolution of Ag atoms to form Ag⁺ ions that subsequently migrate under the action of the applied electric field in correspondence of NW junctions. The electromigration is responsible for the reconfiguration (alteration of the structure and morphology) of NW junctions, with consequent change in the NW junction resistance²⁴, and in the end to the change in the NWN conductivity distribution probed by ERT. Low-resistance junctions can sustain currents of tens of μA each^{23,28}, which is also consistent with our data for \mathcal{V}_c (see maximum excitation currents for \mathcal{V}_c in Table 1).

When performing an ERT measurement with the \mathcal{I}_c protocol, $\max(V^{\text{src}})$ is not under control; in fact the onset of the alterations (marker \downarrow in Fig. 4), occurring at $E = 3.6 \text{ mJ}$, corresponds to a maximum applied voltage, for the whole set of N electrode configurations, $\max(V^{\text{src}}) = 240 \text{ mV}$. The protocol \mathcal{V}_c allows to choose a V^{src} below the damage threshold and at the same time to maximize E , consequently maximizing the signal to noise ratio of the measured transresistance set \mathbf{R} and hence the quality of the ERT reconstruction.

Methods

Metallic nanowire network synthesis. The investigated NWN were synthesized starting from Ag NWs (Sigma-Aldrich, prod. no. 739448) of length $20 \mu\text{m}$ to $50 \mu\text{m}$, diameter $115 \pm (15) \text{ nm}$, coated with $1\text{--}2 \text{ nm}$ of PVP²⁴ and concentration $0.5 \text{ wt.}\%$ in isopropyl alcohol (IPA). By the dilution of the original suspension by additional IPA we obtained NWN of AMD in the range between 70 mgm^{-2} and 120 mgm^{-2} (calculated). NWs were dispersed on a square quartz substrate of size $1 \times 1 \text{ cm}^2$. A detailed structural and chemical characterisation of these nanostructures is reported in our previous work²³.

ERT measurements. The measurement setup used in the present work allows to contact $1 \times 1 \text{ cm}^2$ samples on rigid insulating substrates without any lithographic step. The sample is contacted by 16 gold-coated spring-mounted needle probes (FIXTEST GmbH, model 820.05.01.015) on a circular spot of $\approx 40 \mu\text{m}$ in diameter. The sample is placed in a custom contact fixture and kept in place with an engraved plastic block. A rail-mounted mechanism is actuated to push the sample against the probe-array and achieve electric contact⁹. The probes are arranged along the sample edge (at $500 \mu\text{m}$ distance from it) as shown in Fig. 1b. The inter-probe spacing is 2 mm . Calibrated commercial instrumentation is used to perform the electrical measurements. A Keithley 2602B source-meter is used to generate I_{ij}^{src} or V_{ij}^{src} (and measure the other parameter); an Agilent 34461A voltmeter measures $V_{k,l}^{\text{sense}}$. An Agilent 34980A mainframe, provided with a reed relay module 34933A is used to route the source-meter and voltmeter connections to the various contact configurations i, j, k, l according to the chosen measurement excitation pattern. To minimize electrical stresses on the sample, in particular when the \mathcal{I}_c protocol is chosen, each individual configuration i, j, k, l is reached by setting I^{src} (or V^{src}) to zero, by operating a make-before-break switching, then setting back I^{src} (or V^{src}) to the desired value I (or V) to perform the measurement. (See Supplementary S1 for a detailed ERT measurement setup schematic and thorough description of the adjacent measurement pattern).

For each measurement configuration i, j, k, l , eight measurements were performed and averaged, by reversing each time the excitation and sensing polarity in order to minimize instrument offset and noise. The total time (excitation and instruments switching) of a complete cycle of 208 ERT measurements was 275 s . The measurement setup is hosted in a controlled temperature laboratory at $(22 \pm 1)^\circ\text{C}$, with a relative humidity of $(51 \pm 5)\%$.

ERT modelling. ERT map reconstruction considers a continuous medium having a spatial conductivity function σ ; the typical resolution of the reconstruction is of the order of the electrode spacing. The NWN considered are discontinuous at the scale of the wire interconnections ($< 10 \mu\text{m}$) but can be safely considered continuous at the scale of the map resolution (around the mm); more details are given in Supplementary S4 using arguments from the related literature^{37,38}.

ERT is an ill-posed inverse problem, sensitive to experimental noise in the input data. For this reason, the problem 3 is regularised by an additional term, resulting in

$$\sigma = \arg \min_{\zeta} (||\mathbf{R}_{\text{calc}}(\zeta) - \mathbf{R}||^2 + \lambda ||\mathbf{L}(\zeta)||^2), \quad (7)$$

where λ is the *regularization parameter*, a scalar used to set the amount of regularization.

Equation (7) must be solved numerically. We employed the open source function library EIDORS 3.7.1, which runs on MATLAB^{39,40}. A two-dimensional, finite element model (FEM) of the sample was generated, with the contacts modeled as points corresponding to mesh nodes. $\mathbf{L}(\zeta)$ is given by the EIDORS' regularisation matrix Laplace_prior, which implements an approximation of the second derivative of ζ . To select λ with an objective criterion we used the L-curve method^{41,42}. The FEM model, having \mathbf{R} as input data, is solved for ζ with an absolute-type Gauss-Newton an absolute-type Gauss-Newton inverse solver. The conductivity maps shown in this work were obtained interpolating the FEM solution σ to a square grid of 100×100 pixels. The number of pixels was chosen to be not less than the FEM elements in the mesh (9554) in order to avoid interpolation artifacts.

Conclusions

Electrical Resistance Tomography is usually performed using a constant current \mathcal{I}_c protocol. This protocol is not suitable for characterisation of NWN, since it can induce changes in the sample, due to polarization, even at low excitation levels. We showed that a constant voltage excitation protocol \mathcal{V}_c can be successfully employed to perform ERT maps on NWN without observable sample alteration. The protocol allows to maximize the sample excitation energy E , and hence the signal to noise ratio, for maximum ERT performance.

A quantification of the sample alteration during measurement can be obtained by considering an asymmetry index ν of the impedance matrix \mathbf{Z} .

The measurement procedure and criteria identified can be employed also in the characterisation of other types of NWN and other samples⁴³ and in the ERT of other samples sensitive to damages due to excessive electrical excitation.

Received: 29 June 2020; Accepted: 4 June 2021

Published online: 23 June 2021

References

1. Borcea, L. Electrical impedance tomography. *Inverse Prob.* **18**, R99–R136. <https://doi.org/10.1088/0266-5611/18/6/201> (2002).
2. Holder, D. S. (ed.) *Electrical impedance tomography: Methods, history and applications* (CRC Press, Boca Raton, 2004).
3. Wang, M., Wang, Q. & Karki, B. Arts of electrical impedance tomographic sensing. *Philos. Trans. R. Soc. A: Math. Phys. Eng. Sci.* **374**, 20150329. <https://doi.org/10.1098/rsta.2015.0329> (2016).
4. Brown, B. H., Barber, D. C. & Seagar, A. D. Applied potential tomography: Possible clinical applications. *Clin. Phys. Physiol. Meas.* **6**, 109–121. <https://doi.org/10.1088/0143-0815/6/2/002> (1985).
5. Daily, W., Ramirez, A., LaBrecque, D. & Nitao, J. Electrical resistivity tomography of vadose water movement. *Water Resour. Res.* **28**, 1429–1442. <https://doi.org/10.1029/91wr03087> (1992).
6. Djamdji, F. *et al.* Electrical impedance tomography applied to semiconductor wafer characterization. *Meas. Sci. Technol.* **7**, 391. <https://doi.org/10.1088/0957-0233/7/3/021> (1996).
7. Baltopoulos, A., Polydorides, N., Pambaguian, L., Vavouliotis, A. & Kostopoulos, V. Damage identification in carbon fiber reinforced polymer plates using electrical resistance tomography mapping. *J. Compos. Mater.* **47**, 3285–3301. <https://doi.org/10.1177/0021998312464079> (2013).
8. Cultrera, A. & Callegaro, L. Electrical resistance tomography of conductive thin films. *IEEE Trans. Instrum. Meas.* **65**, 2101–2107. <https://doi.org/10.1109/TIM.2016.2570127> (2016).
9. Cultrera, A. *et al.* Mapping the conductivity of graphene with Electrical Resistance Tomography. *Sci. Rep.* **9**, 10655. <https://doi.org/10.1038/s41598-019-46713-8> (2019).
10. Russo, S., Nefti-Meziani, S., Carbonaro, N. & Tognetti, A. Development of a high-speed current injection and voltage measurement system for electrical impedance tomography-based stretchable sensors. *Technologies* **5**, 48. <https://doi.org/10.3390/technologies5030048> (2017).
11. Sanniccolo, T. *et al.* Electrical mapping of silver nanowire networks: A versatile tool for imaging network homogeneity and degradation dynamics during failure. *ACS Nano* **12**, 4648–4659. <https://doi.org/10.1021/acsnano.8b01242> (2018).
12. Hu, L., Kim, H. S., Lee, J.-Y., Peumans, P. & Cui, Y. Scalable coating and properties of transparent, flexible, silver nanowire electrodes. *ACS Nano* **4**, 2955–2963. <https://doi.org/10.1021/nn1005232> (2010).
13. Hecht, D. S., Hu, L. & Irvin, G. Emerging transparent electrodes based on thin films of carbon nanotubes, graphene, and metallic nanostructures. *Adv. Mater.* **23**, 1482–1513. <https://doi.org/10.1002/adma.201003188> (2011).
14. Ye, S., Rathmell, A. R., Chen, Z., Stewart, I. E. & Wiley, B. J. Metal nanowire networks: The next generation of transparent conductors. *Adv. Mater.* **26**, 6670–6687. <https://doi.org/10.1002/adma.201402710> (2014).
15. Guo, C. F. & Ren, Z. Flexible transparent conductors based on metal nanowire networks. *Mater. Today* **18**, 143–154. <https://doi.org/10.1016/j.mattod.2014.08.018> (2015).
16. Cho, S. *et al.* Large-area cross-aligned silver nanowire electrodes for flexible, transparent, and force-sensitive mechanochromic touch screens. *ACS Nano* **11**, 4346–4357. <https://doi.org/10.1021/acsnano.7b01714> (2017).
17. Zhu, Y. *et al.* Flexible transparent electrodes based on silver nanowires: Material synthesis, fabrication, performance, and applications. *Adv. Mater. Technol.* **4**, 1900413. <https://doi.org/10.1002/admt.201900413> (2019).
18. Sanniccolo, T. *et al.* Metallic nanowire-based transparent electrodes for next generation flexible devices: A review. *Small* **12**, 6052–6075. <https://doi.org/10.1002/sml.201602581> (2016).
19. Sun, Y. *et al.* Flexible organic photovoltaics based on water-processed silver nanowire electrodes. *Nat. Electron.* **2**, 513–520. <https://doi.org/10.1038/s41928-019-0315-1> (2019).
20. Papanastasiou, D. T. *et al.* Transparent heaters: A review. *Adv. Funct. Mater.* **2020**, 1910225. <https://doi.org/10.1002/adfm.201910225> (2020).
21. Won, P. *et al.* Stretchable and transparent kirigami conductor of nanowire percolation network for electronic skin applications. *Nano Lett.* **19**, 6087–6096. <https://doi.org/10.1021/acs.nanolett.9b02014> (2019).
22. Manning, H. G. *et al.* Emergence of winner-takes-all connectivity paths in random nanowire networks. *Nat. Commun.* **9**, 3219. <https://doi.org/10.1038/s41467-018-05517-6> (2018).
23. Milano, G., Porro, S., Valov, I. & Ricciardi, C. Recent developments and perspectives for memristive devices based on metal oxide nanowires. *Adv. Electron. Mater.* **5**, 1800909. <https://doi.org/10.1002/aelm.201800909> (2019).
24. Milano, G. *et al.* Brain-inspired structural plasticity through reweighting and rewiring in multi-terminal self-organizing memristive nanowire networks. *Adv. Intell. Syst.* **2**, 2000096. <https://doi.org/10.1002/aisy.202000096> (2020).
25. Nirmalraj, P. N. *et al.* Manipulating connectivity and electrical conductivity in metallic nanowire networks. *Nano Lett.* **12**, 5966–5971. <https://doi.org/10.1021/nl303416h> (2012).
26. Tu, K. N. Recent advances on electromigration in very-large-scale-integration of interconnects. *J. Appl. Phys.* **94**, 5451–5473. <https://doi.org/10.1063/1.1611263> (2003).
27. Stahlmecke, B. *et al.* Electromigration in gold and single crystalline silver nanowires. *Appl. Phys. Lett.* **88**, 053122. <https://doi.org/10.1063/1.2173533> (2006).
28. Bellew, A. T., Manning, H. G., da Rocha, C. G., Ferreira, M. S. & Boland, J. J. Resistance of single Ag nanowire junctions and their role in the conductivity of nanowire networks. *ACS Nano* **9**, 11422–11429. <https://doi.org/10.1021/acsnano.5b05469> (2015).
29. Adler, A., Gaggero, P. O. & Maimaitijiang, Y. Adjacent stimulation and measurement patterns considered harmful. *Physiol. Meas.* **32**, 731–744. <https://doi.org/10.1088/0967-3334/32/7/s01> (2011).
30. Carletti, C., Montante, G., Westerlund, T. & Paglianti, A. Analysis of solid concentration distribution in dense solid-liquid stirred tanks by electrical resistance tomography. *Chem. Eng. Sci.* **119**, 53–64. <https://doi.org/10.1016/j.ces.2014.07.049> (2014).
31. Milano, G. *et al.* Mapping time-dependent conductivity of metallic nanowire networks by electrical resistance tomography toward transparent conductive materials. *ACS Appl. Nano Mater.* **3**, 11987–11997. <https://doi.org/10.1021/acsnm.0c02204> (2020).
32. Liu, Q. *et al.* Ultra-sharp and surfactant-free silver nanowire for scanning tunneling microscopy and tip-enhanced raman spectroscopy. *Nanoscale* **11**, 7790–7797 (2019).
33. van der Pauw, L. J. A method of measuring the resistivity and Hall coefficient on lamellae of arbitrary shape. *Philips Tech. Rev.* **20**, 220–224 (1958).

34. Lagrange, M. *et al.* Optimization of silver nanowire-based transparent electrodes: Effects of density, size and thermal annealing. *Nanoscale* **7**, 17410–17423 (2015).
35. Buttiker, M. Symmetry of electrical conduction. *IBM J. Res. Dev.* **32**, 317–334 (1988).
36. Zhao, J., Sun, H., Dai, S., Wang, Y. & Zhu, J. Electrical breakdown of nanowires. *Nano Lett.* **11**, 4647–4651. <https://doi.org/10.1021/nl202160c> (2011).
37. Forró, C., Demkó, L., Weydert, S., Voros, J. & Tybrandt, K. Predictive model for the electrical transport within nanowire networks. *ACS Nano* **12**, 11080–11087. <https://doi.org/10.1021/acsnano.8b05406> (2018).
38. Venezian, G. On the resistance between two points on a grid. *Am. J. Phys.* **62**, 1000–1004. <https://doi.org/10.1119/1.17696> (1994).
39. Polydorides, N. & Lionheart, W. R. A Matlab toolkit for three-dimensional electrical impedance tomography: a contribution to the electrical impedance and diffuse optical reconstruction software project. *Meas. Sci. Technol.* **13**, 1871 (2002).
40. Adler, A. & Lionheart, W. R. B. EIDORS: Towards a community-based extensible software base for EIT. In *Proceedings of the 6th Conference on Biomedical Applications of Electrical Impedance Tomography, London* (2005).
41. Hansen, P. C. & O’Leary, D. P. The use of the L-curve in the regularization of discrete ill-posed problems. *SIAM J. Sci. Comput.* **14**, 1487–1503 (1993).
42. Cultrera, A. & Callegaro, L. A simple algorithm to find the L-curve corner in the regularisation of ill-posed inverse problems. *IOP SciNotes* **2020**, 025004. <https://doi.org/10.1088/2633-1357/abad0d> (2020).
43. Huang, Q., Lilley, C. M. & Divan, R. An in-situ investigation of electromigration in Cu nanowires. *Nanotechnology* **20**, 075706. <https://doi.org/10.1088/0957-4484/20/7/075706> (2009).

Acknowledgements

This work is part of the European project “GRACE—Developing electrical characterisation methods for future graphene electronics”, code 16NRM01. This project has received funding from the European Metrology Programme for Innovation and Research (EMPIR) programme co-financed by the Participating States and from the European Union’s Horizon 2020 research and innovation programme.

Author contributions

A.C. and G.M. conceived and conducted the experiment(s), A.C., G.M., and L.C. analysed the results. All authors contributed to write and review the manuscript.

Competing interests

The authors declare no competing interests.

Additional information

Supplementary Information The online version contains supplementary material available at <https://doi.org/10.1038/s41598-021-92208-w>.

Correspondence and requests for materials should be addressed to A.C.

Reprints and permissions information is available at www.nature.com/reprints.

Publisher’s note Springer Nature remains neutral with regard to jurisdictional claims in published maps and institutional affiliations.



Open Access This article is licensed under a Creative Commons Attribution 4.0 International License, which permits use, sharing, adaptation, distribution and reproduction in any medium or format, as long as you give appropriate credit to the original author(s) and the source, provide a link to the Creative Commons licence, and indicate if changes were made. The images or other third party material in this article are included in the article’s Creative Commons licence, unless indicated otherwise in a credit line to the material. If material is not included in the article’s Creative Commons licence and your intended use is not permitted by statutory regulation or exceeds the permitted use, you will need to obtain permission directly from the copyright holder. To view a copy of this licence, visit <http://creativecommons.org/licenses/by/4.0/>.

© The Author(s) 2021